

## Article

# Nonlinear Control Strategies for Enhancing the Performance of DFIG-Based WECS under a Real Wind Profile

Hamid Chojaa <sup>1,\*</sup>, Aziz Derouich <sup>1</sup>, Mohammed Taoussi <sup>1</sup>, Seif Eddine Chehaidia <sup>2</sup>, Othmane Zamzoum <sup>1</sup>, Mohamed I. Mosaad <sup>3,\*</sup>, Ayman Alhejji <sup>3</sup> and Mourad Yessef <sup>4</sup>

<sup>1</sup> Industrial Technologies and Services Laboratory, Higher School of Technology, Sidi Mohamed Ben Abdellah University, Fez 30000, Morocco

<sup>2</sup> Industrial Mechanics Laboratory, Badji Mokhtar Annaba University, P.O. Box 12, Annaba 23000, Algeria

<sup>3</sup> Yanbu Industrial College (YIC), Alnahdah, Yanbu Al Sinaiyah, Yanbu 46452, Saudi Arabia

<sup>4</sup> Laboratory of Engineering, Modeling and Systems Analysis, SMBA University, Fez 30000, Morocco

\* Correspondence: hamid.chojaa@usmba.ac.ma (H.C.); habibm@rcyci.edu.sa (M.I.M.)

**Abstract:** Wind speed variations affect the performance of the wind energy conversion systems (WECSs) negatively. This paper addressed an advanced law of the backstepping controller (ABC) for enhancing the integration of doubly fed induction generator (DFIG)-based grid-connected WECS under wind range of wind speed. This enhancement was achieved through three control schemes, which were blade pitch control, rotor-side control, and grid-side control. The blade pitch control was presented to adjust the wind turbine speed when the wind speed exceeds its rated value. In addition, the rotor and grid-side converter controllers were presented for improving the direct current link voltage profile and achieving maximum power point tracking (MPPT) under speed variations, respectively. To evaluate the effectiveness of the proposed ABC control, a comparison between PI and sliding-mode control (SMC) was presented, considering the parameters of a 1.5 MW DFIG wind turbine in the Assilah zone in Morocco. Moreover, some changes in the DFIG parameters were introduced to investigate the robustness of the proposed controller under parameter uncertainties. Simulation results showed the capability of the proposed ABC controller to enhance the performance of the DFIG-WECS based on variable speed and variable pitch turbine, at both below and above-rated speed, leading to an error around  $10^{-3}$  (p.u), with an ATE = 0.4194 in the partial load region; in terms of blade pitch control, an error of  $2 \cdot 10^{-4}$  (p.u) was obtained, and the DC-link voltage profile showed a measured performance of 5 V and remarkable THD value reduction compared to other techniques, with a measured THD value of 2.03%, 1.67%, and 1.46% respectively, in hypynchronous, hypersynchronous, and pitch activation modes of operation. All simulations were performed using MATLAB/SIMULINK based on real wind profiles in order to make an exhaustive analysis with realistic operating conditions and parameters.

**Keywords:** adaptive backstepping control; doubly fed induction generator; field orientation control; MPPT by curve fitting; pitch control; wind energy in Morocco



**Citation:** Chojaa, H.; Derouich, A.; Taoussi, M.; Chehaidia, S.E.; Zamzoum, O.; Mosaad, M.I.; Alhejji, A.; Yessef, M. Nonlinear Control Strategies for Enhancing the Performance of DFIG-Based WECS under a Real Wind Profile. *Energies* **2022**, *15*, 6650. <https://doi.org/10.3390/en15186650>

Academic Editors: Salah Kamel, Omar Hazem Mohammed and Mohammed Kharrich

Received: 8 August 2022

Accepted: 2 September 2022

Published: 12 September 2022

**Publisher's Note:** MDPI stays neutral with regard to jurisdictional claims in published maps and institutional affiliations.



**Copyright:** © 2022 by the authors. Licensee MDPI, Basel, Switzerland. This article is an open access article distributed under the terms and conditions of the Creative Commons Attribution (CC BY) license (<https://creativecommons.org/licenses/by/4.0/>).

## 1. Introduction

The harmful impact of fossil fuels on the environment and their fast depletion all over the world make the free-pollution transition imperative. Electrical energy generation through wind turbines is the most viable energy source due to its daily availability [1,2]. North African countries aspire to become world leaders in the production and exportation of clean energy thanks to their geographical location, the presence of strong sun irradiation for long periods, and the availability of wind at a relatively high speed, especially in the northern coastal areas overlooking the Mediterranean Sea. Among these nations, the Kingdom of Morocco has more wind energy potential. The extreme north of the country (Tangier, Tetouan), the Essaouira region, the southern Atlantic zone from Tarfaya to Lagouira, and the zone between the Atlas mountain ranges and the Rif are the four most

profitable zones to explore wind energy [1]. The wind power generated in these regions does not exceed 10 GW, which is not consistent with the unique location of these regions in terms of wind availability with speeds that may exceed 6.5 m/s and attain (10 m/s). Hence, integrating some modern control strategies into the wind energy systems can increase the level of wind power generated in these zones [3].

The classical PI controller presents appropriate performances in many WECS applications. Optimized PI controllers were presented to improve the performance of the WECS [4,5]. Due to its limitations, in particular, the inability to adapt to machine parameter variations and uncertainties, any change in the operating conditions other than the one with which the PI controller parameters were optimized would not guarantee optimal operation. This called for real-time PI controller parameter tuning depending on the variation of wind speed and the possible parametric variations, due in practice to technical problems (e.g., mechanical component wear, overheating of the machine). In practice, the implementation of such techniques is still difficult and costly, as the CPU takes time to adjust the optimal parameter and needs an advanced microprocessor. These limitations in PI and/or optimized PI controllers have led to the implementation of some robust and adaptive control techniques for WECSs. More robust control strategies were proposed to replace PI controllers to improve accuracy and precision performances [6]. The sliding-mode controller (SMC) is robust against uncertainties, but its performance is undermined by high-frequency low oscillations called chattering. An SMC also utilizing sliding-mode control for grid-side converters and rotor-side converters of a DFIG in WECS application was presented to dampen the sun-synchronous fault event [7]. Improved versions of the SMC such as super-twisting SMC [8,9] and second-order SMC [10], with very attractive dynamic features such as finite time convergence, have been proposed in the literature to reduce the chattering phenomenon. Another nonlinear adaptive controller, the energy-shaping L2-gain controller, was presented to the WECS without adding any flexible devices to improve the WECS performance [11]. Other control schemes were presented without using flexible devices to improve the DFIG-WECS performance such as the linear quadratic regulator controller [12] and fuzzy logic controller [13]. Advanced versions of the backstepping controller (ABC) such as integral and adaptive backstepping have been proven to be robust against parameter variation and system uncertainties as in [14,15].

Fixed-speed wind turbines have several demerits with more expensive power converters such as low energy efficiency and reduced lifespan because of high mechanical stress [16]. Variable-speed wind turbine-driven doubly fed induction generators (DFIGs) are gradually being introduced to deal with these inconveniences. According to S. Karad and colleagues [17], the DFIG has occupied 50% of the total installed capacity, making it the predominating type of machine in the wind energy market. This DFIG's dominance is due to its benefits, which include ease of use, grid and generator control, and active and reactive power regulation capabilities. Furthermore, because DFIG rotor converters can be rated to sustain only the slip power, which is one-third of the total nominal power of the generator, the total cost of installation and maintenance is lower [5,18]. The DFIG can also harvest energy from a wider range of wind speeds, which is  $\pm 30\%$  of the synchronous speed. The DFIG's principal disadvantage when used in WECS, on the other hand, is its susceptibility to grid disturbance events and variations in operating conditions including wind speed. Wind speed variation had negative effects on the performance and operation of DFIG-WECS [19]. These negative effects included the mechanical stress on the DFIG rotor, the deviation from the maximum extraction of the power operating point, and variations in the DC-link voltage. The mechanical stress may damage the DFIG rotor and not operating at the maximum power point decreases the efficiency of the system, while large variations in the DC-link voltage may destroy the DC-link capacitance or disconnect the generator from the system by the protection devices [1].

Collective pitch control (CPC) and individual pitch control (IPC) are the two categories of pitch angle control techniques. The CPC is currently applied to wind turbines in the market and involves measuring a single pitch angle to control the inclination of the three

blades as one entity. It relies on a simple controller, such as the PI controller as proposed in [20,21], fuzzy PI that was presented in [22], and sliding-mode control that was also successfully used in the literature to regulate the turbine pitch angle [23]. The IPC is the most recent development which has been intensively treated in the last years, but it is still not completely implemented in commercial wind turbines (WT) [24]. It is expected to be largely applied in the next generation of turbines to usher in the era of larger and more flexible blades to reduce the load and stress on the turbine system. The disadvantage of the IPC, however, is that it renders the pitch system an inherently multiple-input-multiple-output (MIMO) system, since it requires individual pitch commands for each blade and thereby requires additional sensors for pitch angle feedback measurement of each blade.

In order to alleviate the effect of wind speed variation and maximize the harvesting of the power generated from DFIG-WECS, the MPPT technique through controlling the rotor-side converter of the generator is widely used at the machine side [25]. However, on the turbine side, the tip-speed-ratio method is used. It consists of controlling the rotor speed to keep the relative speed at its optimum value by acting on the electromagnetic torque signal [26]. Optimal torque control (OTC) consists of adapting the electromagnetic torque  $T_{em}$  to its optimum value without the need to measure the wind speed [26]. The optimum value of the torque can be determined in two ways. The first method is based on some approximations, such as neglecting the effect of viscous friction and the hypothesis that the wind speed varies very slowly in the steady-state operation compared to the electrical time constants of the wind turbine system [27]. The optimal torque can then be obtained as a function of generator speed. The second method is based on the use of an optimal torque speed lookup table. With this method, estimating the generator torque may be required [28]. The disadvantage of this OTC technique is that characterization tests are required offline to design the lookup table. In general, both OTC and power signal feedback (adapting power instead of torque) are simple, fast, and efficient. However, efficiency is lower compared to that of the relative velocity method because it does not measure the wind speed directly, meaning that wind changes are not reflected instantaneously and significantly on the reference signal [25,28]. Both OTC and power signal feedback algorithms have the same drawbacks during the MPP tracking under low wind speeds for large-inertia WTs, although they are robust and cost-effective algorithms [26]. The fuzzy MPPT search algorithm features several advantages such as quick response, low oscillations around the MPP, wind speed measurements not being needed, and accurate WECS mathematical modeling not being needed, and depends solely on the measurement of generator speed and output power [29]. However, it still requires the designer's best knowledge in specifying the suitable surface error, levels of membership functions, and choosing the rule-base layer, and it demands considerable memory space allocation [30].

The wind speed variation affects the value of the DC-link voltage and consequently causes some oscillations in the power generated from the WECS. Regulating this voltage retains the nominal value of the generated power and dampens the oscillations in both the DC-link voltage and the power generated. Optimal PI and fractional-order PI controllers for keeping the DC-link voltage at the reference value during wind speed variations and wind gusts were presented in the reference [31]. To successfully control the rotor-side power converter (RSPC) and grid-side power converter (GSPC), the DFIG mathematical model was transformed to a d-q reference frame using different transformation schemes such as stator voltage orientation (SVO) or stator flux orientation (SFO) [32] and air gap flux [33]. The SVO employed in [32] enabled the direct and quadrature components of the rotor and filter current to be controlled independently. Important research works on vector control have been carried out where the orientation schemes have been combined successfully with the PI regulator [32,34], sliding-mode controller [35,36], backstepping controller [37], and fuzzy logic to control the DFIG-based WT [38]. One can also see a comparative study of different types of controllers applied for DFIG-WECS in the reference [6]. The SMC was presented for only MPPT of a WECS-based DFIG as in [25,26]. Backstepping, as an adaptive controller, was presented to limit the rotor current of a DFIG in wind systems to support

fault ride-through [27]. The DC link of the DFIG was not investigated in this study despite the vital role of this link in controlling the reactive power flow between the generator and the grid. The backstepping controller was also used for DFIG wind systems for optimal control of the generator speed only [34]. Another application of this adaptive controller was investigated for the speed control of a DFIG [35]. Each of these studies [25–27,34,35] used SMC and backstepping to achieve a specific goal but could not enumerate the goals achieved by these adaptive controls. To fill the gap between using these adaptive controllers to perform more than one goal in addition to enhancing the backstepping controller, this paper presented three different goals for DFIG-based wind systems.

This paper presented three control schemes to mitigate the effects of wind speed variation on DFIG-WECS. These control schemes were pitch angle control, RSPC, and GSPC of the DFIG. The control of the DFIG-based wind energy converter was designed with a focus on the wind profile obtained from the Assilah region of Morocco. The aim was to improve the power quality, maximize turbine energy efficiency, optimize the robustness of controller performance, and increase the ease of implementation. The conducted comparative study was carried out based on the four control strategies under the wind speed profile obtained from Assilah. The main objectives of this article were:

- For the MPPT controller to calculate the optimal generator speed that leads to the maximum power point as the wind speed changes.
- For the pitch angle controller to ensure that the captured mechanical power is below the generator nominal power.
- For the RSPC controller to act on the inverters to track the optimum speed and desired stator reactive power.
- For the GSPC controller, the objectives were to keep the DC-bus voltage constant and annul the reactive power generated by the filter.
- To study the robustness of the proposed controller under parameter uncertainties through some changes in the DFIG parameters.
- To evaluate and compare the ABC designed to control the RSPC to PI and SMC in terms of precision, response time, robustness, and output power quality.

The rest of this paper is organized as follows: Section 2 gives an overview and modeling of the grid-connected DFIG. The pitch, MPPT, and RSPC controllers are carefully elaborated in Section 3. Simulation results from MATLAB/Simulink are presented and discussed in Section 4. Finally, a short conclusion is presented in Section 5.

## 2. System Overview and Modeling

Figure 1 describes the four zones in the evolution of extracted mechanical power in a function of incident wind speed. In zone one, the wind speed is less than the minimum speed  $v_{min}$  (corresponds to minimum power  $P_{min}$ ) needed to start the turbine.

The turbine is on a partial load in zone 2, where the objective is to capture as much energy as possible. Maximum energy efficiency is ensured by a maximum power coefficient through the maximum power point tracking (MPPT). When the wind speed exceeds its nominal value  $v_n$  (wind speed corresponding to the nominal power), the turbine is in zone 3 and on full load. The objective here is to limit the power captured to its nominal value  $P_n$ . The wind generator is controlled by varying the pitch angle in order to produce this nominal power as long as the maximum wind speed that the structure of the wind turbine can tolerate is not yet reached.

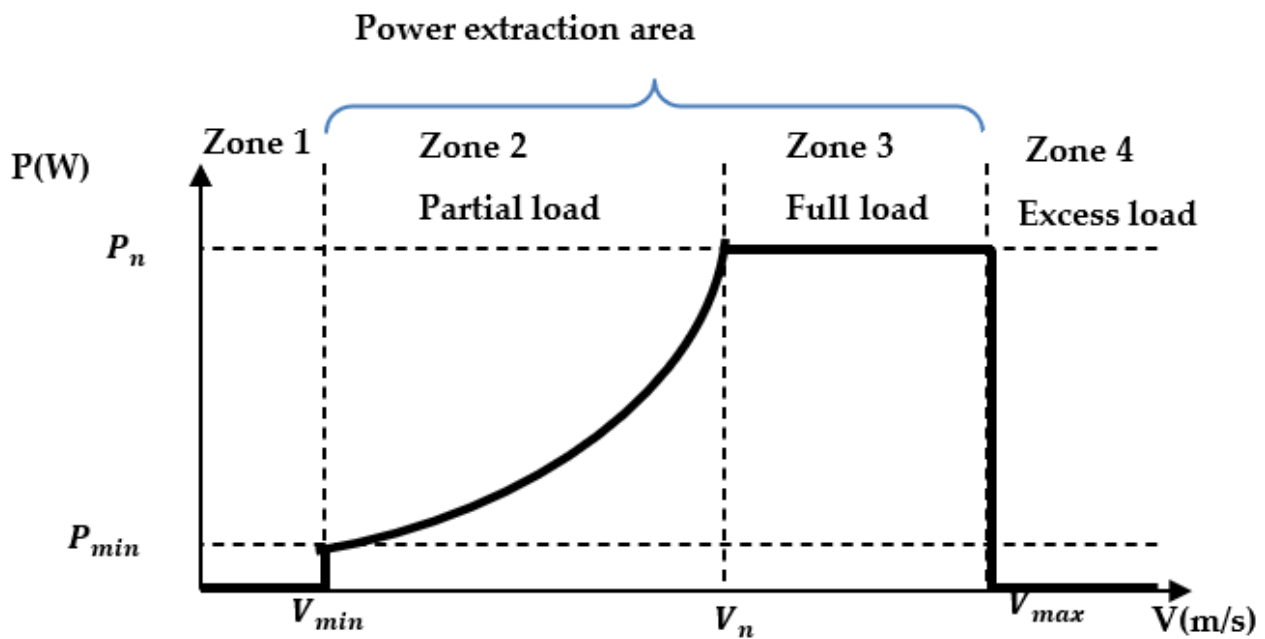


Figure 1. Operating zones of the wind turbine [22].

The overall grid-connected wind turbine described in Figure 2 comprises a doubly fed induction generator connected to the utility grid directly through its stator. The rotor windings are linked to the back-to-back power converters made up of the rotor-side power converter (RSPC), DC-link capacitor, and the grid-side power converter (GSPC). The other side of the back-to-back converter is connected to the grid via the grid filters. The rotor shaft of the DFIG is coupled to that of the prime mover (three-blade turbine) through the gearbox. Moreover, the prime mover driven by a moving mass of wind captures a fraction of the kinetic energy in the wind and converts it to mechanical energy on the generator shaft through the gearbox. The mechanical energy on the rotor shaft is converted to electrical energy by the DFIG and transferred to the utility grid through the stator or both depending on the mode of operation. Technically, the back-to-back converter pulse-width modulation power converter allows for a bidirectional power flow control. As a result, the DFIG can operate either in the sub-synchronous or in the super-synchronous mode [39]. In detail, in the synchronous mode/super-synchronous mode, the generator rotor rotates at synchronous speed, and the energy is transferred to the grid through the stator alone. In the sub-synchronous mode, the generator's speed of rotation is below the synchronous speed, energy is transferred to the grid through the stator, and the slip energy is absorbed from the grid by the rotor windings. The super-synchronous mode transfers energy to the grid via the rotor (slip energy) and the stator.

## 2.1. Turbine Modeling

### 2.1.1. Aerodynamics

The mathematical expression of the mechanical power  $P_t$  extracted by the turbine is described in (1) in the function of the power coefficient  $C_p$ , air density  $\rho$ , area of the circular surface with turbine blades' length as radius  $S$ , and the speed of a moving mass of wind  $v$ .  $C_p$  expressed in (2) is the power conversion coefficient of the turbine (Figure 3). It depends on the angle of inclination of the blades called the pitch angle  $\beta$  and the tip speed ratio (TSR)  $\lambda$  [1,2]. When the wind speed is beyond the rated speed, the pitch angle adjusts to curtail the effect of extreme wind speed on the generated power [40].

$$P_t = C_p P_w = \frac{1}{2} C_p(\lambda, \beta) \rho S v^3 \quad (1)$$

$$C_p(\lambda, \beta) = c_1 \left( \frac{c_2}{\lambda_i} - c_3\beta - c_4 \right) e^{-\frac{c_5}{\lambda_i}} + c_6\lambda_i \quad (2)$$

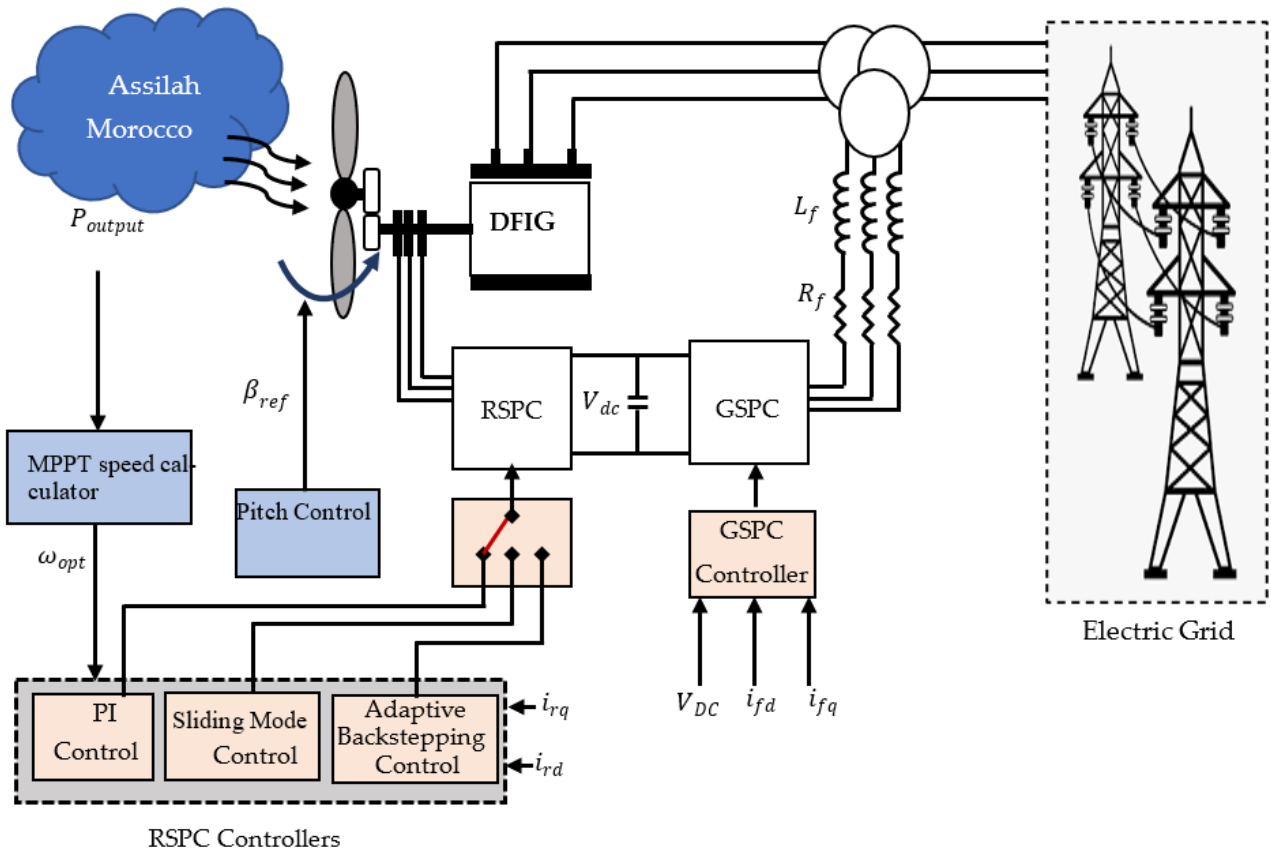


Figure 2. General overview of DFIG linked to the grid.

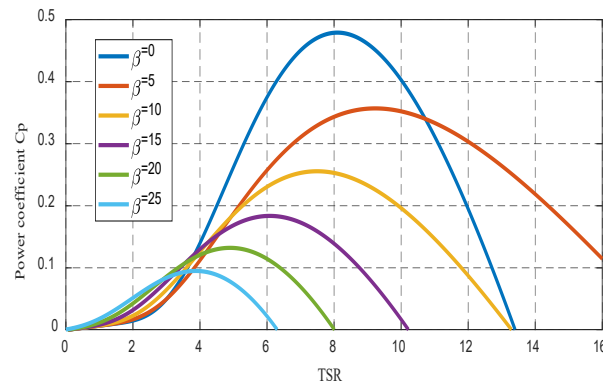


Figure 3. Power efficiency for different pitch angles and TSR.

The constants  $c_1, c_2, c_3, c_4, c_5,$  and  $c_6$  are given in the Appendix A,  $\frac{1}{\lambda_i} = \frac{1}{\lambda + 0.08\beta} - \frac{0.035}{\beta^3 + 1}$ , and:

$$\lambda = \frac{R\omega_t}{v} \quad (3)$$

$$T_t = \frac{P_t}{\omega_t} = \frac{\pi}{2\lambda} \rho R^3 v^2 C_p(\lambda, \beta) \quad (4)$$

### 2.1.2. Dynamics

The two-mass model is used to describe the dynamic equations of the turbine and generator shafts in the function of inertias, speed, and torques as illustrated in (5) and (6) [40].

$$2H_t \frac{d\omega_t}{dt} = T_t - T_{shaft} \quad (5)$$

$$2H_m \frac{d\omega_g}{dt} = T_{em} + T_{shaft} \quad (6)$$

The torque on the rotor shaft, in terms of shaft stiffness  $K_{sh}$  and damping constant  $D$  and TSR, are expressed in (7).

$$T_{shaft} = K_{sh} \int (\omega_t - \omega_g) dt + D(\omega_t - \omega_g) \quad (7)$$

### 2.2. Model of the Rotor-Side Power Converter

The dynamic model of the DFIG in the d-q synchronous reference frame with an angular speed of  $\omega_s$  is expressed in (8) through (12) [15,40]. Equation (8) illustrates stator and rotor fluxes.

$$\left\{ \begin{aligned} \varphi_{sd} &= L_s i_{sd} + L_m i_{rd} & \varphi_{sq} &= L_s i_{sq} + L_m i_{rq} \\ \varphi_{rd} &= L_r i_{rd} + L_m i_{sd} & \varphi_{rq} &= L_r i_{rq} + L_m i_{sq} \end{aligned} \right. \quad (8)$$

Equation (9) describes the voltage across both windings:

$$\left\{ \begin{aligned} v_{sd} &= R_s i_{sd} + \frac{d\varphi_{sd}}{dt} - \omega_s \varphi_{sq} & v_{sq} &= R_s i_{sq} + \frac{d\varphi_{sq}}{dt} + \omega_s \varphi_{sd} \\ v_{rd} &= R_r i_{rd} + \frac{d\varphi_{rd}}{dt} - \omega_r \varphi_{rq} & v_{rq} &= R_r i_{rq} + \frac{d\varphi_{rq}}{dt} + \omega_r \varphi_{rq} \end{aligned} \right. \quad (9)$$

The slip speed  $\omega_r$  is given in (10), such as:

$$\omega_r = \omega_s - p \cdot \omega_g \quad (10)$$

The resultant  $T_{em}$  is expressed in (11) in terms of rotor winding currents and stator flux.

$$T_{em} = \frac{3}{2} p \frac{L_m}{L_s} (\varphi_{sq} i_{rd} - \varphi_{sd} i_{rq}) \quad (11)$$

Equation (12) describes stator and rotor active and reactive power as a function of currents and voltages as follows:

$$\left\{ \begin{aligned} P_s &= \frac{3}{2} (v_{sd} i_{sd} + v_{sq} i_{sq}) & Q_s &= \frac{3}{2} (v_{sq} i_{sd} - v_{sd} i_{sq}) \\ P_r &= \frac{3}{2} (v_{rd} i_{rd} + v_{rq} i_{rq}) & Q_r &= \frac{3}{2} (v_{rq} i_{rd} - v_{rd} i_{rq}) \end{aligned} \right. \quad (12)$$

To decouple the control of d and q components of the rotor current, a phase-locked loop (PLL) is implemented to achieve stator voltage orientation (SVO), where the d-axis of the reference frame is aligned to the stator voltage position. The q component of the stator voltage is consequently null ( $v_{sq} = 0$ ). If the grid is assumed to be of fixed frequency, the derivatives of stator fluxes  $\varphi_{sq}$  and  $\varphi_{sd}$  are also null (constant flux). Due to the high power of generators employed in wind turbines, stator resistance is negligible. The direct component of stator voltage can hence be deduced as  $v_{sd} = -\omega_s \varphi_{sq}$ . Rotor current dynamics necessary for controller synthesis can then be deduced from (8) and (9) and expressed in (13) and (14).

$$\frac{di_{rd}}{dt} = \frac{v_{rd}}{\sigma L_r} - \frac{R_r i_{rd}}{\sigma L_r} + e_{rd} \quad (13)$$

$$\frac{di_{rq}}{dt} = \frac{v_{rq}}{\sigma L_r} - \frac{R_r i_{rq}}{\sigma L_r} + e_{rq} \quad (14)$$

where  $\sigma = 1 - \frac{L_m^2}{L_s L_r}$ ,  $e_{rd} = \omega_r i_{rq} + \frac{L_m \omega_r \varphi_{sq}}{\sigma L_r L_s}$ , and  $e_{rq} = -\omega_r i_{rd}$ .  $T_{em}$  and stator power equations from (11) and (12) can then be given under SVO as:

$$T_{em} = \frac{3}{2} p \frac{L_m}{L_s} (\varphi_{sq} i_{rd}) \tag{15}$$

$$\left\{ P_s = -\frac{3}{2} \frac{L_m}{L_s} v_{sd} i_{rd} \quad Q_s = -\frac{3}{2} \frac{v_{sd}}{L_s} (\varphi_{sq} - L_m i_{rq}) \right. \tag{16}$$

### 2.3. Model of the Grid-Side Power Converter

The d-axis and q-axis components of the current-transiting filter in SVO can be expressed as (17) and (18).

$$\frac{di_{fq}}{dt} = -\frac{R_f}{L_f} i_{fq} + e_{fq} - \frac{v_{fq}}{L_f} \tag{17}$$

$$\frac{di_{fd}}{dt} = -\frac{R_f}{L_f} i_{fd} + e_{fd} - \frac{v_{fd}}{L_f} \tag{18}$$

where the coupling terms are defined as:

$$e_{fq} = -\omega_s i_{fd}, \quad e_{fd} = -\omega_s i_{fq} + \frac{v_{sd}}{L_f}$$

The equations in (19) represent the active and reactive power exchanged between the grid and the filter.

$$\left\{ P_f = \frac{3}{2} (v_{sd} i_{fd}) \quad Q_f = -\frac{3}{2} (v_{sd} i_{fq}) \right. \tag{19}$$

The dynamics of the DC-link voltage can be obtained by analyzing the instantaneous active power at the DC bus. The relationship linking capacitor active power  $P_c$ , filter active power  $P_f$ , rotor active power  $P_r$ , and the total power loss in the RSPC and GSPC  $P_{loss}$  is given in (20).

$$P_c = P_f - P_r - P_{loss} \tag{20}$$

In this work,  $P_{loss}$  was considered to be negligible. Following the filter active power expressions from (19) and the voltage dynamics across the capacitor expressed in (21), where  $i_{ond}$  was direct in this work,  $P_{loss}$  was considered to be negligible. Substituting the filter active power expressions (19) into (20), the derivative of the capacitor voltage is represented in (21), where  $i_{ond}$  is the direct current transition from the capacitor to the RSPC.

$$V_{dc} \frac{dV_{dc}}{dt} = \frac{3v_{sd} i_{fq}}{2C} - V_{dc} i_{ond} \tag{21}$$

## 3. Control Strategy

### 3.1. Curve Fitting MPPT Control (Optimum Speed Calculation)

Figure 4 illustrates the evolution of extracted power in a function of rotor speed when wind speed varies. It can be observed that each curve is characterized by a peak characterized by the optimum speed and maximum power obtainable at that wind speed.

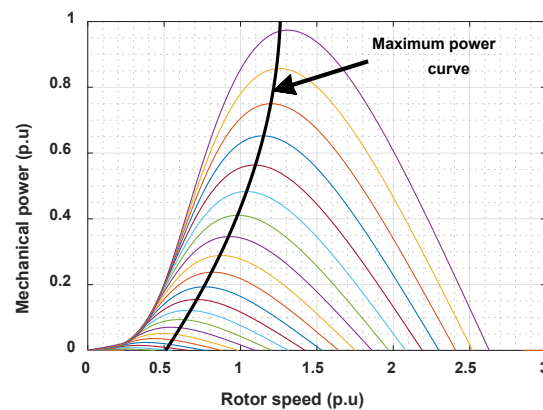


Figure 4. MPPT by curve fitting.

The objective of the MPPT block in Figure 1 is to dynamically calculate the generator speed that places the operating point at the tip of the power curve. Several techniques such as relative speed, best torque, power, perturb and observe, and fuzzy logic controls have been employed in the literature [26]. To enjoy the advantage of rapidity and ease of implementation, a curve-fitting strategy was adopted in this paper to provide the optimum rotor speed from active power measurement by, first of all, plotting the maximum power curve as illustrated in Figure 4, where the performance curve of wind turbine are given for various pitch angles. The curve covers the habitual operating area of the turbine ( $0.7p.u \leq \omega_g \leq 1.3p.u$  and  $0p.u \leq P \leq 1p.u$ ). The best mathematical description of the maximum power curve obtained is expressed in (22), such as:

$$\omega_{opt} = -0.67P^2 + 1.42P + 0.51 \quad (22)$$

where  $\omega_{opt}$  and  $P$  are the optimum generator speed leading to MPP and measured active power, respectively.

### 3.2. Rotor-Side Power Converter Control

Adaptive backstepping controller (ABC), sliding-mode controller (SMC), and proportional–integral controller (PIC) were synthesized separately to achieve zero reactive power at the stator and best rotor speed.

#### 3.2.1. PI Controller (PIC)

The PIC controller synthesized for the RSPC is illustrated in Figure 5, where a faster outer loop controller regulates the generator speed to track the speed supplied by the MPPT block. The output of this outer controller is the reference current for the inner-loop regulator, which in turn controls the current to track the generated current reference to give the final control input  $v_{rd}$ . For the reactive power control, the reference value of the q-axis current is calculated from the reference stator reactive power from (16), and a single PI corrector is applied to control the current.

Figure 6 shows the control technique of the inner-loop rotor currents of the DFIG by the PI regulator. The controller gains are tuned using the classical pole-zero cancellation method based on a specific bandwidth  $w_p$  function of the synchronous speed of the DFIG; more information about the used method are presented in Refs [41]. The terms  $\hat{e}_{rq}$  and  $\hat{e}_{rd}$  in the control algorithm are intended to be precisely equal to the terms  $e_{rq}$  and  $e_{rd}$  in the transfer function of the DFIG to cancel them. If the annulation succeeds, the whole system can be represented by the equation of a first-order system described in (23).

$$F(s) = \frac{1}{\sigma L_r P + R_r} \quad (23)$$

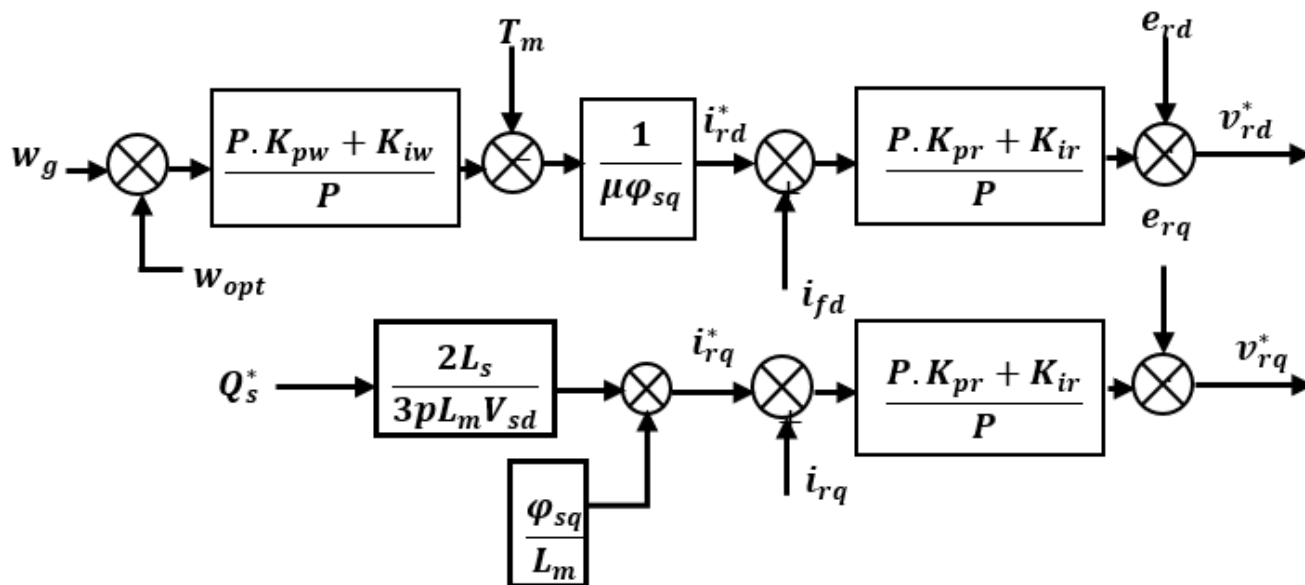


Figure 5. RSPC PI controller setup showing generator speed and stator reactive power control.

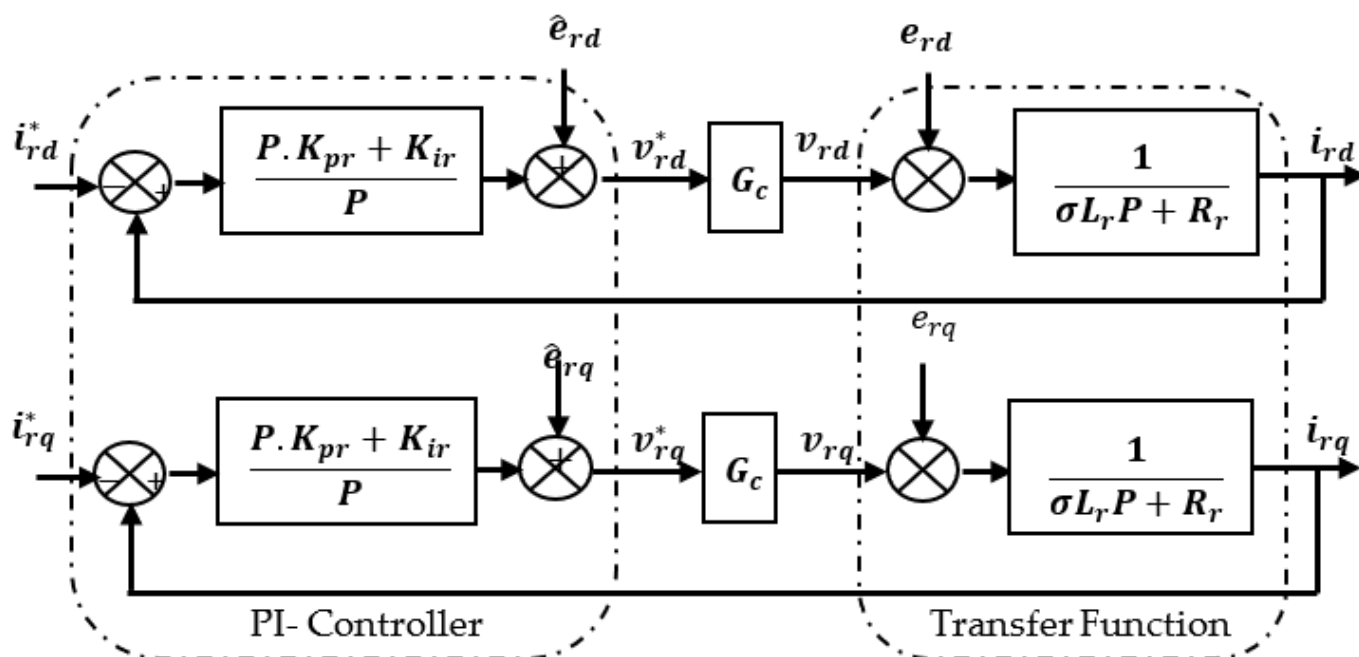


Figure 6. DFIG inner-loop control with transfer function.

A suitable control technique for the system, which would guarantee the tracking of the reference values, would be the PI regulator with its parameters chosen using the pole-zero cancellation technique. Unfortunately, the decoupling terms depend on the intrinsic parameters of the generator and the stator flux. The parameters of the PI controllers also depend on the electrical parameters of the generator. These parameters are not constant due to temperature changes, skin effects, and saturation. The stator flux is no longer constant during network voltage dip. This phenomenon of variation in the parameters and the flux, as well as modeling inaccuracy, reduce the robustness of the PIC.

### 3.2.2. Design of Sliding-Mode Control (SMC)

The SMC is a variable structure control technique whose advantages reside in its simplicity and robustness when faced with system uncertainties and external disturbances.

To ensure the stability of the system, system states are made to track the sliding surface and to slide on the surface until reaching the equilibrium point. It is therefore necessary to define a surface whose characteristics guarantee the attractiveness and stability. Hence, to design an SMC law, the control law, we took the general form proposed by Slotting [25]:

$$S(x) = \left( \frac{d}{dt} + \lambda \right)^{n-1} e(x) \quad (24)$$

$$e = x - x_d \quad (25)$$

where  $e$ : tracking error,  $\lambda$ : a positive coefficient,  $n$ : relative degree,  $x_d$ : reference value, and  $x$ : state variable to be controlled. The proposed control scheme is validated in terms of stability by employing the Lyapunov stability criteria with the choice of the function represented in (26).

$$V(S) = \frac{1}{2} S^2 \quad (26)$$

We must first define a sliding surface, then define the condition of existence of the sliding mode, and finally determine the condition  $\dot{V} < 0$  that must be fulfilled to guarantee the asymptotic stability of the SMC. From (26), the condition of attractiveness represented in (27) is obligatory and enough for the sliding variable  $S(x, t)$  to track 0.

$$\dot{V}(S) = \dot{S} \cdot S < 0 \quad (27)$$

For finite-time convergence, the condition of attractiveness that only guarantees asymptotic convergence is replaced with a more restrictive condition illustrated in (28).

$$\dot{S} \cdot S < -k_d \cdot S \cdot \text{sign}(S); k_d > 0 \quad (28)$$

In the sliding mode and steady state,  $S = 0$  and  $\dot{S} = 0$ . For our system, we defined the sliding surface as in (24), where  $\varepsilon = \varepsilon_\omega = \omega_g - \omega_{opt}$  and  $\varepsilon = \varepsilon_q = i_{rq} - \alpha_q$  for speed and for reactive power control, respectively.

$$S = \dot{\varepsilon} + \lambda \varepsilon \quad (29)$$

The resulting control inputs that ensure the achievement of the RSPC control objectives after SMC synthesis are given in (30) and (31).

$$v_{rd} = \frac{\sigma L_r}{\mu} \left[ -k_d \text{sign}(S) + \frac{f \dot{\omega}_g}{J} - \lambda \varepsilon_\omega + \ddot{\omega}_{opt} \right] + \frac{R_r i_{rd}}{\sigma L_r} - \omega_r i_{rq} - \frac{L_m \omega_r \varphi_{sd}}{\sigma L_r L_s} \quad (30)$$

$$v_{rq} = \sigma L_r \left[ -k_q \text{sign}(\varepsilon_q) + \frac{R_r i_{rq}}{\sigma L_r} + \omega_r i_{rd} + \dot{\alpha}_q \right] \quad (31)$$

### 3.2.3. Adaptive Backstepping Control (ABC)

To render the controller immune to unforeseen perturbations while improving convergence, a term  $\theta$  is added to the state-space equations to account for eventual system uncertainties. The ABC technique iteratively and systematically develops the control input, estimates the uncertainties as  $\hat{\theta}$ , and adapts the control variable accordingly. The error of estimation is defined in (32), where  $\underline{\theta}$  is the estimation error.

$$\underline{\theta} = \theta - \hat{\theta} \quad (32)$$

Considering the incertitude as a constant parameter  $\dot{\theta} = 0$ , the derivative of (32) gives (33).

$$\dot{\underline{\theta}} = -\dot{\hat{\theta}} \quad (33)$$

### Step 1 (Speed Control)

Equation (34) shows the generator's speed tracking error.

$$\varepsilon_\omega = \omega_g - \omega_{opt} \quad (34)$$

The Lyapunov stability approach is employed to ascertain stability and convergence of the error between the actual and reference rotor speed; therefore, the Lyapunov function chosen and presented in (35) takes the speed incertitude estimation error into account and is derived in (36). The condition in (37) was selected to establish that the derivative function is always negative.

$$V_\omega(\varepsilon_\omega) = \frac{1}{2}\varepsilon_\omega^2 + \frac{\theta_\omega^2}{2m_\omega} \quad (35)$$

$$\dot{V}_\omega = \varepsilon_\omega \left( \frac{T_m}{J} - \frac{f\omega_g}{J} - \mu i_{rd} - \dot{\omega}_{opt} \right) + \varepsilon_\omega \dot{\theta}_\omega + \frac{\theta_\omega \dot{\theta}_\omega}{m_\omega} \quad (36)$$

$$\dot{V}_\omega \leq -k_\omega \varepsilon_\omega^2 \quad (37)$$

According to (33) and substituting (36) in (37), the two equalities expressed in (38) are deduced.

$$\left\{ \begin{aligned} -k_\omega \varepsilon_\omega &= \frac{T_m}{J} - \frac{f\omega_g}{J} - \mu i_{rd} - \dot{\omega}_{opt} + \hat{\theta}_\omega \varepsilon_\omega + \frac{\theta_\omega \dot{\theta}_\omega}{m_\omega} = 0 \end{aligned} \right. \quad (38)$$

The reference of the d-axis rotor current is the virtual control input for the next step deduced from the first expression in (38) and expressed in (39).

$$i_{rd}^* = \frac{1}{\mu} \left( k_\omega \varepsilon_\omega + \frac{T_m}{J} - \frac{f\omega_g}{J} - \dot{\omega}_{opt} \right) = \alpha_{rd} \quad (39)$$

The integral of the incertitude can then be obtained from the second expression, and it is given in (40).

$$\dot{\hat{\theta}}_\omega = -m_\omega \varepsilon_\omega \quad (40)$$

### Step 2 (Inner-Loop Current Control)

The tracking error in step 2 represented in (41) is defined as the discrepancy between the d-axis current and its reference value calculated in step 1.

$$\varepsilon_{rd} = i_{rd} - \alpha_{rd} \quad (41)$$

The chosen Lyapunov function to guarantee convergence of the tracking error in step 2 is expressed in (42) and derived in (43) as follows:

$$V_{rd}(V_\omega, \varepsilon_{rd}) = V_\omega + \frac{1}{2}\varepsilon_{rd}^2 + \frac{\theta_{rd}^2}{2m_{rd}} \quad (42)$$

$$\dot{V}_{rd} = -k_\omega \varepsilon_\omega^2 - \mu \varepsilon_\omega \varepsilon_{rd} + \varepsilon_{rd} \dot{\varepsilon}_{rd} + \frac{\theta_{rd} \dot{\theta}_{rd}}{m_{rd}} \quad (43)$$

In order to ensure the stability and convergence of the tracking error, the negativity of the Lyapunov function's first derivative must be verified.

Expression (44) was therefore chosen, where  $k_{rd}$  is a positive control parameter.

$$\dot{V}_{rd} \leq -k_\omega \varepsilon_\omega^2 - k_{rd} \varepsilon_{rd}^2 \quad (44)$$

Equation (44) is valid for the two expressions given in (45).

$$\left\{ \begin{array}{l} -k_{rd}\varepsilon_{rd} = -\mu\varepsilon_\omega + \frac{v_{rd}}{\sigma L_r} - \frac{R_r i_{rd}}{\sigma L_r} + e_{rd} + \hat{\theta}_{rd} - \dot{\alpha}_{rd} \varepsilon_{rd} \theta_{rd} + \frac{\theta_{rd} \dot{\theta}_{rd}}{m_{rd}} = 0 \end{array} \right. \quad (45)$$

From the first equation in (45), the final control input  $v_{rd}$  is deduced and expressed as:

$$v_{rd} = \sigma L_r \left( -k_{rd}\varepsilon_{rd} + \mu\varepsilon_\omega + \frac{R_r i_{rd}}{\sigma L_r} - e_{rd} - \hat{\theta}_{rd} + \dot{\alpha}_{rd} \right) \quad (46)$$

The second expression of (45) leads to Equation (47) from which the integral of the uncertainty can be derived using the derivative block in Simulink to obtain the value of the perturbation.

$$\dot{\hat{\theta}}_{rd} = -m_{rd}\varepsilon_{rd} \quad (47)$$

#### Stator Unity Power Factor Control

The desired value of stator reactive power is usually zero to achieve a unity power factor (UPF) at the stator windings. Therefore, the tracking error chosen and defined in (48) is the difference between the q-axis rotor current and its reference  $\alpha_{rq}$  derived from (16).

$$\varepsilon_{rq} = i_{rq} - \alpha_{rq} \quad (48)$$

Equations (49) and (50) represent the chosen Lyapunov function and its derivative, respectively, considering the uncertainty estimation error.

$$V_{rq}(\varepsilon_{rq}) = \frac{1}{2}\varepsilon_{rq}^2 + \frac{\theta_{rq}^2}{2m_{rq}} \quad (49)$$

$$\dot{V}_{rq} = \varepsilon_{rq} \left( \frac{v_{rq}}{\sigma L_r} - \frac{R_r i_{rq}}{\sigma L_r} + e_{rq} + \hat{\theta}_{rq} - \dot{\alpha}_{rq} \right) + \varepsilon_{rq} \theta_{rq} + \frac{\theta_{rq} \dot{\theta}_{rq}}{m_{rq}} \quad (50)$$

Equation (51) ensures that the first derivative of the Lyapunov function is strictly negative.

$$\dot{V}_{rd} = -k_{rq}\varepsilon_{rq}^2 \quad (51)$$

From (49) and (50), the two expressions deduced and expressed in (52) establish the stability and convergence of  $\varepsilon_{rq}$ .

$$\left\{ \begin{array}{l} -k_{rq}\varepsilon_{rq} = \frac{v_{rq}}{\sigma L_r} - \frac{R_r i_{rq}}{\sigma L_r} + e_{rq} + \hat{\theta}_{rq} - \dot{\alpha}_{rq} \varepsilon_{rq} \theta_{rq} + \frac{\theta_{rq} \dot{\theta}_{rq}}{m_{rq}} = 0 \end{array} \right. \quad (52)$$

The final control variable is then obtained from (52) and presented in (53).

$$v_{rq} = \sigma L_r \left( -k_{rq}\varepsilon_{rq} + \mu\varepsilon_\omega + \frac{R_r i_{rd}}{\sigma L_r} - e_{rd} - \hat{\theta}_{rd} + \dot{\alpha}_{rd} \right) \quad (53)$$

The first derivative of the estimated value of the uncertainty parameter is represented in (54) with the hypothesis that the uncertainty is constant or with slow dynamics.

$$\dot{\hat{\theta}}_{rd} = -m_{rd}\varepsilon_{rd} \quad (54)$$

### 3.3. Filter Reactive Power and DC-Link Voltage Control

The main aim of the grid-side converter control is to maintain the voltage across the capacitor constant and to obtain a unity power factor at the RL filter.

As shown in Figure 7, the controller to keep the voltage across the capacitor at a fixed value is done in two steps with two PI regulators. The first PI controller computes the reference of the d-axis filter current, which ensures the tracking of the DC-link voltage's desired value. This reference is then supplied to the inner-loop control, where the second PI controller is designed to ensure the tracking of this reference input by the direct component of the filter current. The parameters of the two PI controllers are given in Appendix A.

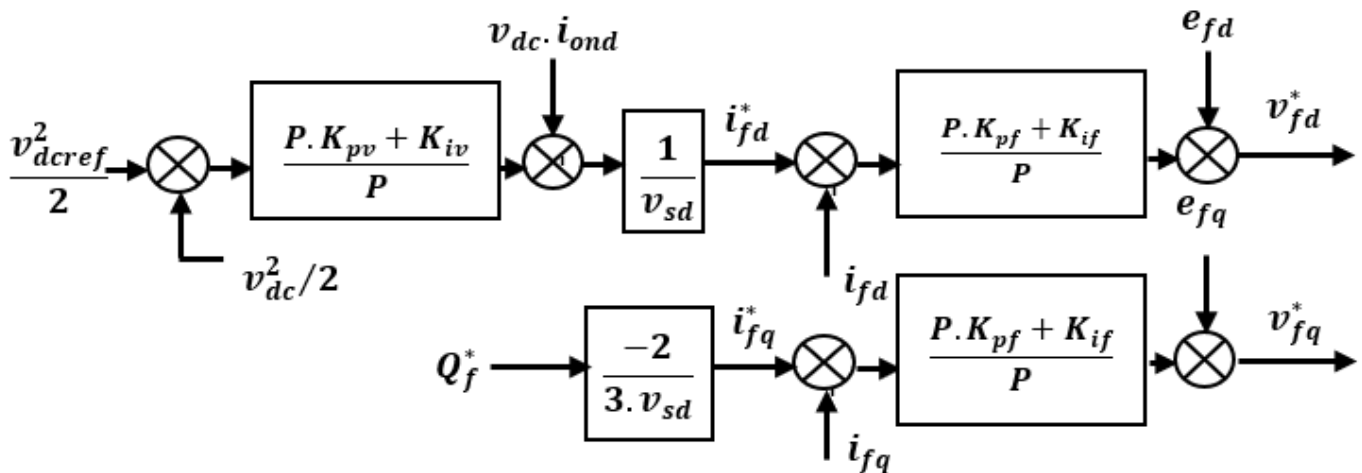


Figure 7. GSPC PIC control strategy showing DC-link voltage and filter reactive power control.

### 3.4. Pitch Angle Control

From Figure 8, it can be observed that an increase in the angle of inclination degrades the efficiency of the turbine, thereby reducing the power captured. Consequently, to ensure that the power captured does not exceed the nominal power of the DFIG, the blade angle of inclination is controlled to deteriorate the efficiency of the turbine by reducing the power captured. In this paper, feedback control of the speed of rotation and the power of the generator using P and PI regulators was proposed and is illustrated in Figure 8 as employed. This technique has the advantage of guaranteeing that both the speed and power do not exceed their respective nominal values.

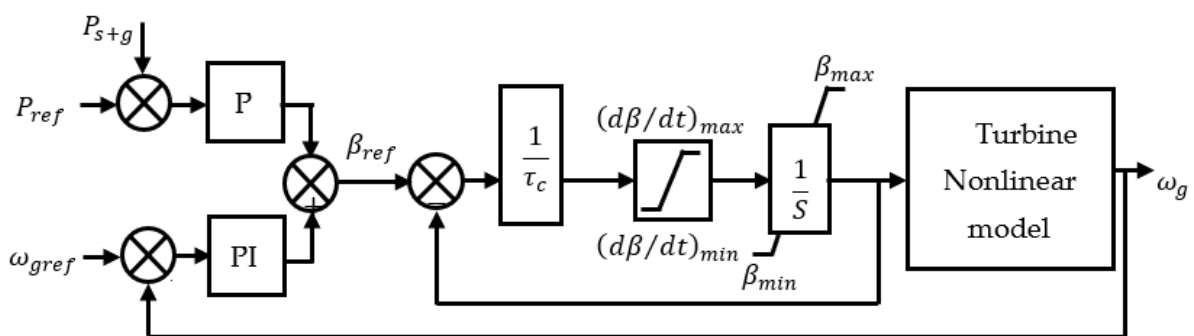
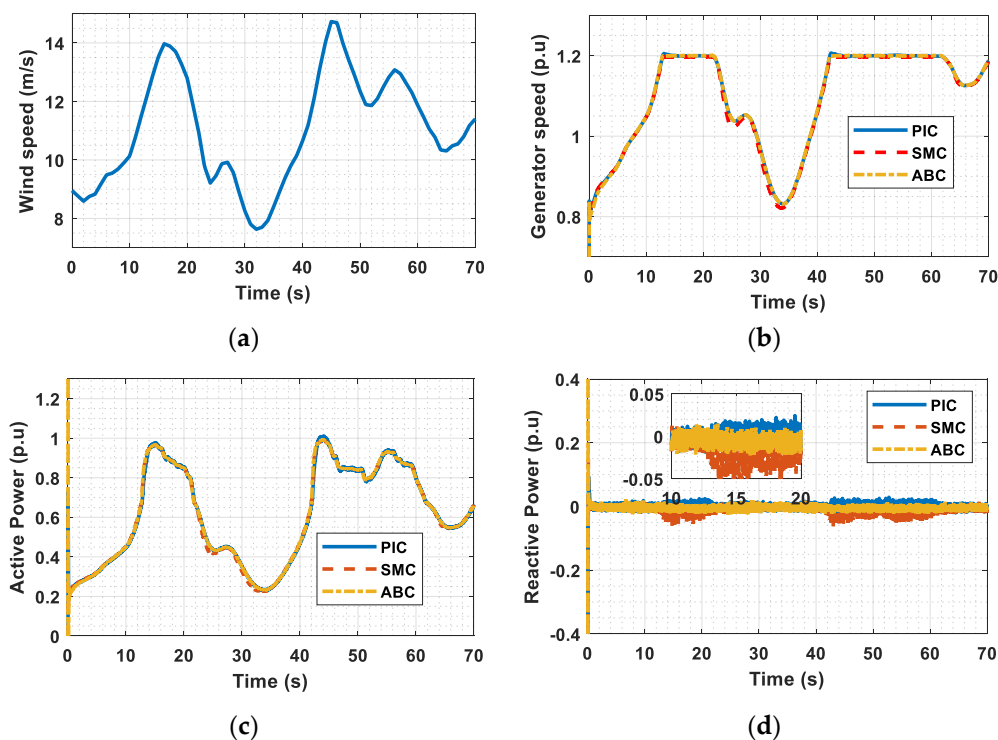


Figure 8. Angle of inclination regulator with model of pitch activation.

## 4. Simulation Results

In this section, the performance of the control strategies employed in this work is evaluated under the real wind speed profile obtained from the Assilah zone in Morocco. The obtained large wind data of several days were truncated to the 70 s wind profile presented in Figure 9a. This range of wind speed was selected to permit the turbine to be examined under all the modes of operation possible. A detailed Simpower model of the DFIG presented in Figure 1 was designed and evaluated under MATLAB/Simulink software. Note that three controllers whose efficiencies were to be compared were designed for the RSPC, while only the PIC was synthesized for the GSPC. The desired values of

filter and stator reactive power were chosen to be zero to guarantee the UPF at the point of common coupling. The optimum generator speed was supplied by the MPPT block, while the reference DC-link voltage was given to be 1150 V. Outcomes of the PIC, SMC, and ABC controllers' simulations are provided and analyzed, and comparisons were made when the turbine was operating in MPPT or at a partial load (hypersynchronous and hypersynchronous modes) and under pitch angle activation modes.



**Figure 9.** Controllers' performances in p.u. (a) Speed of incident wind, (b) Generator speed, (c) PCC Active power, and (d) PCC Reactive power.

The curves represented in Figure 9 are the wind speed in Figure 9a, generator rotational speed in Figure 9b, and DFIG active and reactive powers, respectively, in Figure 9c,d. According to Figure 9, it appears that all the controllers (PIC, SMC, and ABC) had acceptable transient and steady-state performance. However, during the intervals when the pitch angle was activated, the reactive power under the PIC and SMC contained disturbing ripples of about 1%, while the ABC technique remained unperturbed. It can also be observed that the dynamics of the settling times of the speed and active and reactive power dynamics were more attractive under the ABC controller when compared to the two other controllers. Figure 10 presents the controllers' response in real time, the evolution of the pitch angle is shown in Figure 10a, the power coefficient is represented in Figure 10b, the electromagnetic torque is plotted in Figure 10c, and the DC-link voltage evolution is in Figure 10d. As observed in Figure 10a, the pitch activation was executed with more excellent precision under the ABC strategy, as it occurs only at instances when the generator speed exceeds the rated value, and it exhibited smoother evolution during the transient phases. The evolution of the power coefficient presented in Figure 10b confirms that the three controllers responded to the tracking of the power curve tip, as they all tracked the highest conversion efficiency of 0.5. However, the ABC demonstrated the best response time and precision, while the SMC gave the worst precision but better convergence than the PIC. Some deviations observed on the curve at intervals 10 s to 20 s, 40 s to 52 s, and 52 s to 60 s were due to the pitch activation, which deteriorates the power coefficient to lessen the power converted in order to maintain the expected lifespan of the WECS. For the electromagnetic torque, at instances of partial load (no pitch activation), the variation was smoothest under the ABC, which reduces mechanical stress on the drive train, and highest

for the SMC controller due to its associated chattering phenomenon. During the pitch angle activation phases, however, the variations in the electromagnetic torque were more pronounced with the PIC and SMC and more accentuated with the PIC due to its inability to handle the unforeseen perturbation and nonlinearities introduced by the pitch activation. Figure 10d shows that the Vdc waveform with PIC during pitch activation possessed the worst dynamics, as undesirable undulations around the reference values were observed. The quantitative description of these ripples is given in Table 1.

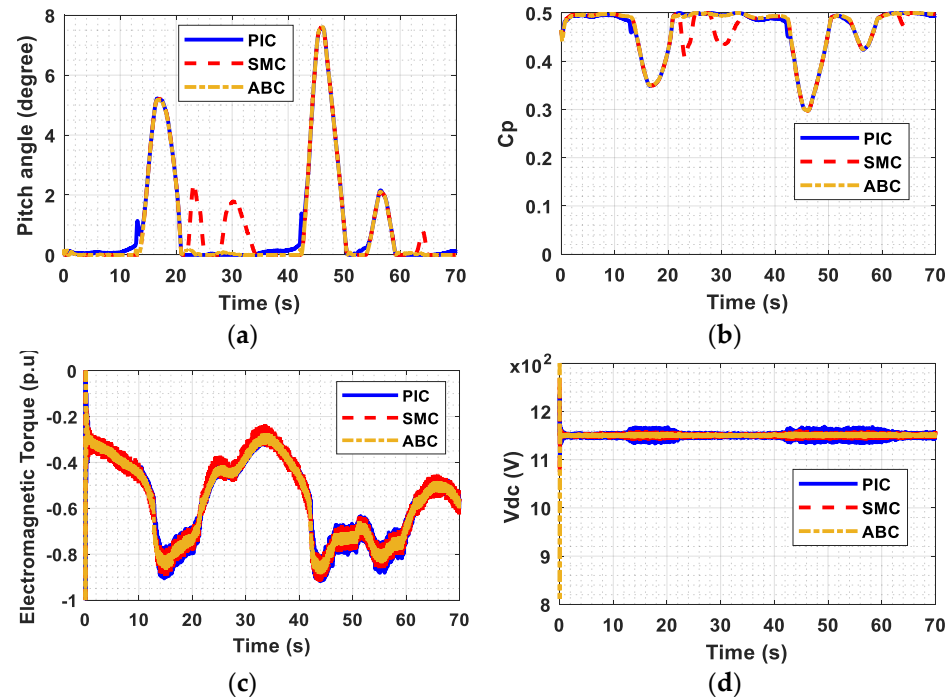


**Figure 10.** Controllers' response in real time; (a) Pitch angle, (b) Power coefficient, (c)  $T_{em}$ , and (d) DC-link voltage.

**Table 1.** Tracking error (ripple).

|                                 | Partial Load               |              |                 | Pitch Activated   |                   |                   |
|---------------------------------|----------------------------|--------------|-----------------|-------------------|-------------------|-------------------|
|                                 | PIC                        | SMC          | ABC             | PIC               | SMC               | ABC               |
| Generator speed $\omega_g$      | $3.54 \cdot 10^{-3}$ (p.u) | 0.012 (p.u)  | $10^{-3}$ (p.u) | $2.10^{-3}$ (p.u) | $2.10^{-3}$ (p.u) | $2.10^{-4}$ (p.u) |
| DC-link voltage $v_{dc}$        | 5.7 (V)                    | 7 (V)        | 4 (V)           | 17 (V)            | 10 (V)            | 5 (V)             |
| Electromagnetic Torque $T_{em}$ | 0.0225 (p.u)               | 0.0415 (p.u) | 0.02 (p.u)      | 0.0525 (p.u)      | 0.0475 (p.u)      | 0.0225 (p.u)      |
| D-axis rotor current $i_{rd}$   | 0.001 (p.u)                |              | 0.001 (p.u)     | 0.09 (p.u)        |                   | 0.01 (p.u)        |
| Q-axis rotor current $i_{rq}$   | 0.015 (p.u)                | 0.02 (p.u)   | 0.019 (p.u)     | 0.24 (p.u)        | 0.16 (p.u)        | 0.02 (p.u)        |

To give a glimpse of the efficiency and precision of the outer and inner loops of the three controllers, waveforms of the tracking errors of generator speed, d-q axes rotor currents, and DC-link voltage are presented in Figure 11. According to Table 1 and Figure 11, the errors which are all less than 0.1% of the reference values when the pitch angle is not activated are acceptable. However, during instances of pitch angle activation, the PIC and SMC recorded the highest undesirable errors which sometimes attained 1% of the reference values.

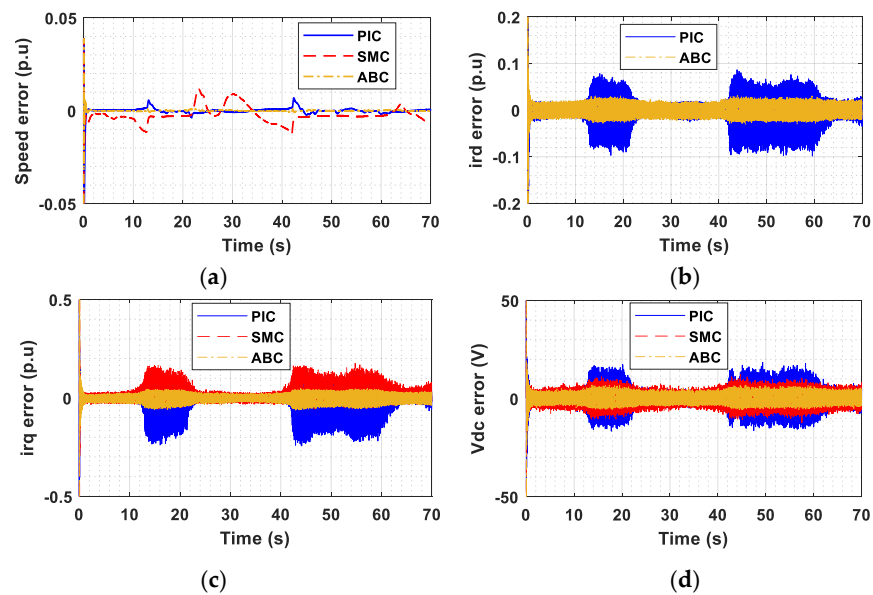


**Figure 11.** Controllers' performance in (p.u.); (a) Generator speed error (b), d-axis rotor current error, (c) q-axis rotor current error, and (d) Capacitor voltage error.

Figures 12–14 illustrate the curves of rotor and stator currents under PIC, SMC, and ABC techniques, respectively. The frequency of rotor current varied depending on the generator speed, while that of the stator remained constant. To further compare the effectiveness of the studied controllers, Figure 15 describes the THD of stator current during 20 cycles from the instant  $t = 64.9$  (s) obtained under the three controllers. SMC exhibited the highest waveform deformation with a THD of 4.20%, followed by PIC which had 2.86%. The best waveform conformity was obtained under the ABC controller with an acceptable THD of 1.67%. To further study and compare the suitability of the waveforms of the currents transferred to the grid and to avoid erroneously generalizing the performance of the controllers through THD values taken only at 64.95 s, THD values under the three controllers during hyposynchronous, hypersynchronous, and pitch activation modes of operation were obtained and are displayed on the bar chart presented in Figure 16 for proper comparison. The same trend could be observed during hyposynchronous and hypersynchronous operations, where the THD was always highest with SMC and lowest with ABC. The highest THD of 6.46%, however, was obtained with PIC during pitch activation operation. THD with ABC was always lowest during the three modes of operation, with its best THD of 1.46% obtained during pitch activation mode. It is therefore obvious that the ABC provided the most desirable performance in terms of stator current harmonic distortion.

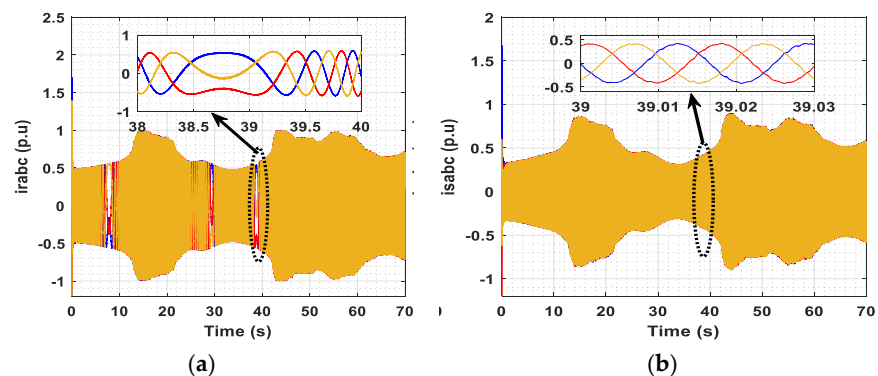


**Figure 12.** (a) Rotor current, (b) stator current waveforms under PIC.

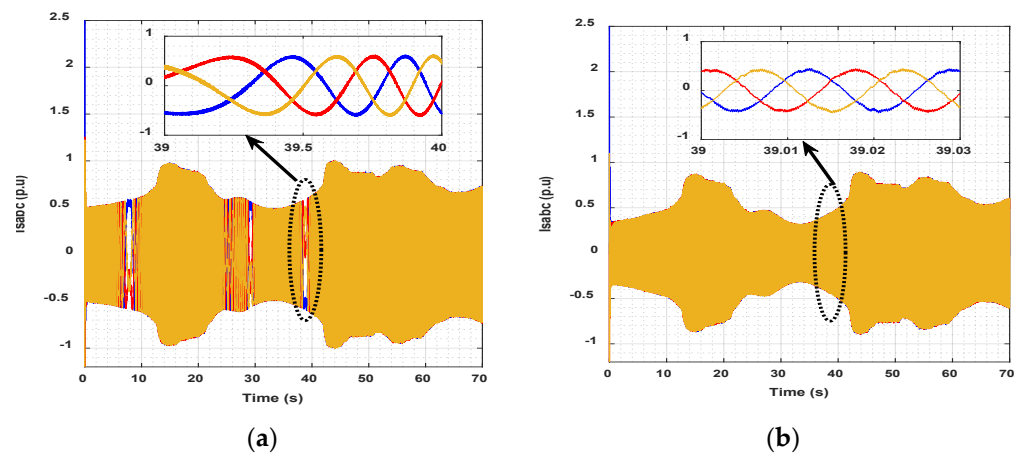


Figure 13. (a) Rotor current, (b) stator current waveforms under SMC.

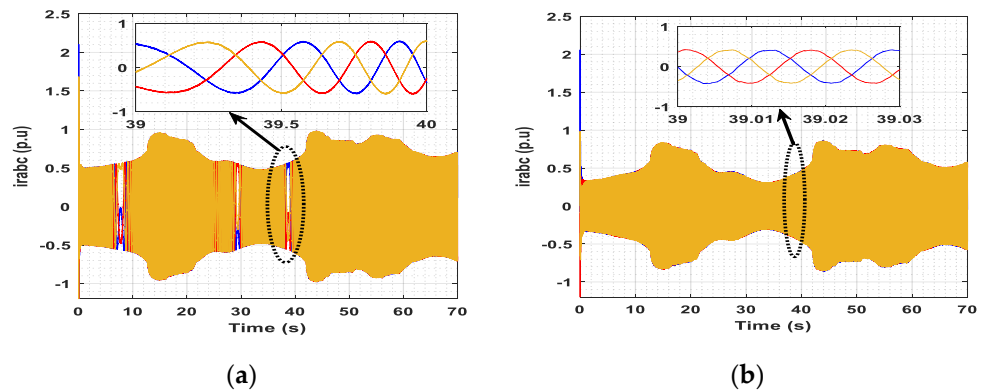


Figure 14. (a) Rotor current, (b) stator current waveforms under ABC.

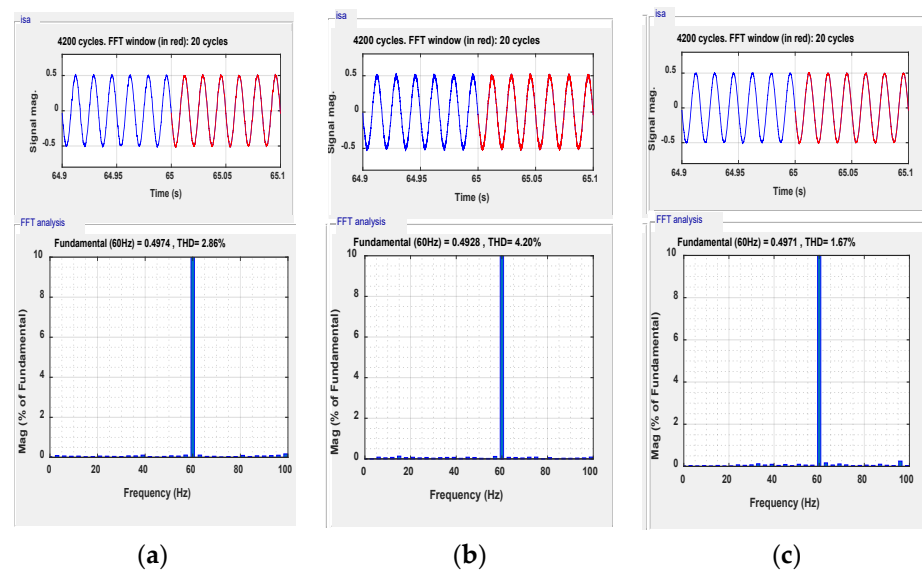
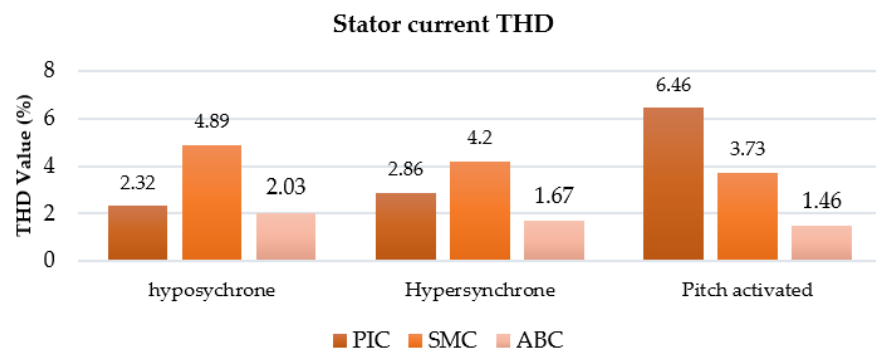


Figure 15. Stator current total harmonic distortion (THD) under: (a) PIC, (b) SMC, and (c) ABC.



**Figure 16.** Bar graph showing stator current THD under: PIC, SMC, and ABC in hyposynchronous, hypersynchronous, and pitch activation modes of operation.

To assess the performance of the three controllers presented in this work in terms of precision, this paper adopted the most popularly used index ITAE [32], defined in (55).

$$ITAE = \int t|\varepsilon|dt \quad (55)$$

The smaller the ITAE, the more attractive the controller performance. The quantitative results for generator speed, DC-link voltage, and q-axis and d-axis rotor currents are presented in Table 2. It can be noted from Table 2 that the ABC controller had minimum values of ITAE compared to SMC and PIC schemes. Therefore, the proposed ABC controller provided the best performance and excellent tracking.

**Table 2.** ITAE of PIC, SMC, and ABC errors.

|                               | PIC   | SMC   | ABC    |
|-------------------------------|-------|-------|--------|
| Generator speed $\omega_g$    | 9.141 | 9.141 | 0.4194 |
| DC-link voltage $v_{dc}$      | 6305  | 4403  | 3126   |
| D-axis rotor current $i_{rd}$ | 32.34 |       | 12.64  |
| Q-axis rotor current $i_{rq}$ | 76.71 | 41.69 | 26.67  |

In order to further examine and compare the robustness of the three controllers, another series of simulations were carried out to test the effect of step variations in the intrinsic parameters of the DFIG. In the first evaluation, a step increase of 50% in stator and rotor resistances was introduced simultaneously at  $t = 10$  s while the wind speed was kept constant at 8 m/s. The resulting rotor current convergence errors are plotted in Figure 17, where it can be observed that the three control schemes exhibited excellent robustness and ensure satisfactory steady-state performance even in the presence of parametric variations.

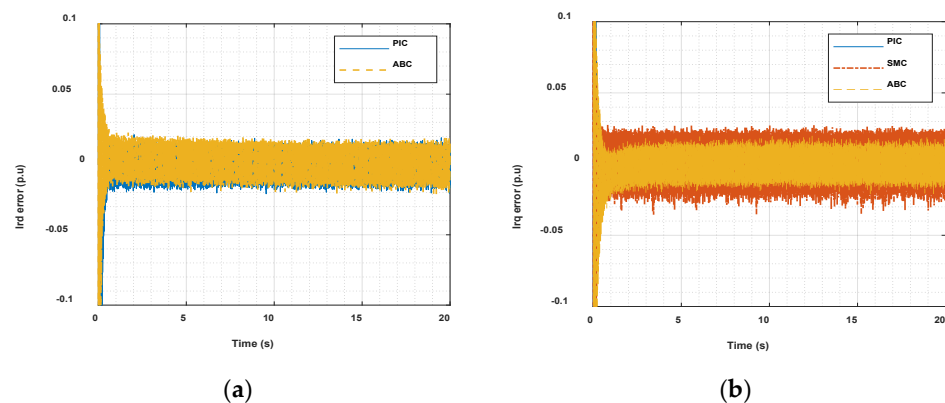


**Figure 17.** Rotor current error under 50% step increase in rotor and stator resistances; (a) Direct, (b) quadrature.

The second simulation was performed under the same scenarios but with the addition of a 50% step increase in the rotor, stator, and mutual inductances at  $t = 10$  s. Figure 18 shows that at the instance of parameter variation, the curves of current-tracking errors featured spikes of up to 0.12 p.u. However, ABC appeared to be the best with almost smooth curves and good tracking of set-point curves, followed by the command based on the PI regulators, which presented rapid settling time. Then, the SMC gave remarkable and superior ripples compared to those obtained by the other two commands, which were still able to attenuate oscillations under parametric variations of the machine.

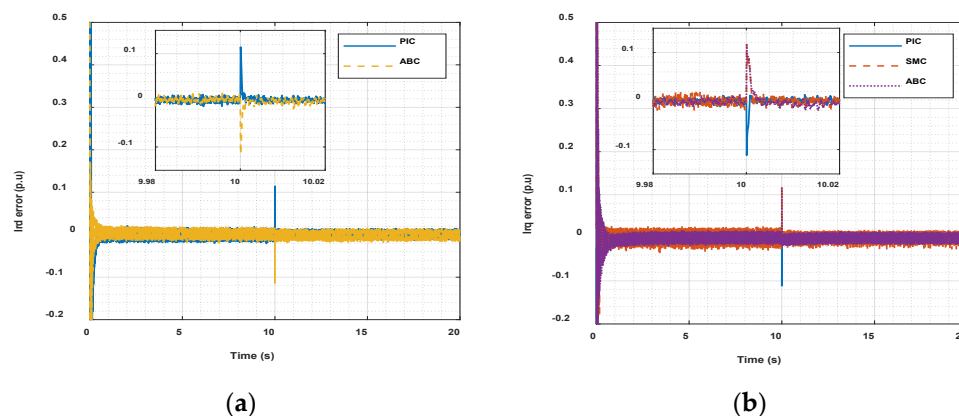


**Figure 18.** Rotor current error under 50% step increase in rotor and stator resistances, inductances, and mutual inductance; (a) Direct, (b) quadrature.

## 5. Conclusions

This paper presented detailed modeling and control strategies for a grid-connected DFIG wind turbine system intended for installation in sites with the real wind speed profile of Assilah City, Morocco. The analytical technique designed to track the tip of the power curve allows for minimization of the number of sensors needed in the installation, facilitates the implementation of advanced control laws, and decreases the maximum power point calculation time. The PI corrector-based pitch angle controller's efficiency is improved through both speed and output power feedback to guarantee the safe operation of the turbine under wind gusts. PIC, SMC, and ABC coupled with stator voltage orientation were designed to track MPP and achieve the UPF. Those controllers were analyzed and compared in terms of precision, where ABC gave the best tracking error around  $10^{-3}$  (p.u.), with an ATE = 0.4194, fast response time, current waveform suitability, target tracking, and simplicity. Moreover, the presented controller strategies performed well in a high-speed condition, where the speed regulation in the pitch zone recorded an error of around  $2.10^{-4}$  (p.u). Regarding other indicators, the measured errors of  $T_{em}$ ,  $i_{rd}$ , and  $i_{rq}$  were, respectively, 0.0225, 0.01, and 0.02 (p.u). Further, the robustness of the proposed controller against system uncertainties was presented by changing the rotor and stator resistances and inductances. Simulation results proved that the three control strategies realized the MPPT and the UPF. However, under system disturbances such as the activation of the pitch controller, ABC proved to be the most suitable with a very good precision, fast response time, excellent efficiency, and robustness.

In practice, all presented control strategies can be implemented in wind farms. However, as reported by [42], the integration of wind farms increases system nonlinearities interpreted by the mean of additional fluctuations to the frequency signal. To mitigate the effect of coupling and connection time delay, an additional load frequency control should be added [43]. Research into solving this problem is already underway to make an exhaustive investigation of the application of the proposed controller in the present manuscript.

**Author Contributions:** Conceptualization, H.C., A.D. and S.E.C.; methodology, H.C., A.D., S.E.C. and M.I.M.; software, H.C. and S.E.C.; validation, H.C., S.E.C. and M.I.M.; formal analysis, H.C., A.D., M.T., S.E.C., O.Z., M.I.M., A.A. and M.Y.; resources, H.C., A.D., S.E.C. and M.I.M.; data curation, H.C., S.E.C., M.I.M. and A.A.; writing—original draft preparation, H.C.; writing—review and editing, S.E.C., O.Z. and M.I.M.; visualization, H.C., A.D., M.T., S.E.C., O.Z., M.I.M., A.A. and M.Y.; supervision, A.D., S.E.C. and M.I.M.; project administration, A.D. All authors have read and agreed to the published version of the manuscript.

**Funding:** This research received no external funding.

**Institutional Review Board Statement:** Not applicable.

**Informed Consent Statement:** Not applicable.

**Data Availability Statement:** Not applicable.

**Conflicts of Interest:** The authors declare no conflict of interest.

### Abbreviation

|                                     |   |
|-------------------------------------|---|
| $P_t$                               | Turbine Power                                     |
| $C_p, C_{pmax}$                     | Efficiency and maximum efficiency                 |
| $\lambda, \lambda_{opt}$            | Tip Speed Ratio (TSR) and best TSR                |
| $\beta$                             | Blade angle of inclination (pitch)                |
| $\rho$                              | Air Density                                       |
| $S$                                 | Area of circle created by rotating turbine blades |
| $v, v_{est}, v_{est}$               | Actual and estimated wind speeds                  |
| $\omega_t, \omega_g$                | turbine and rotor speed                           |
| $R$                                 | Length of turbine blade                           |
| $T_t, T_{test}$                     | turbine torque                                    |
| $G$                                 | Gear ratio  |
| $T_{shaft}$                         | Mechanical Torque                                 |
| $T_{em}$                            | Electromagnetic Torque                            |
| $K_{sh}, D$                         | Shaft stiffness and damping constant              |
| $p$                                 | number of machine pole pairs                      |
| $i_{sd}, i_{sq}$                    | Stator current d and q components                 |
| $i_{rd}, i_{rq}$                    | Rotor current d and q components                  |
| $\varphi_{sd}, \varphi_{sq}$        | Stator flux d and q components                    |
| $\varphi_{rd}, \varphi_{rq}$        | Rotor flux d and q components                     |
| $\omega_r, \omega_s$                | Slip speed and angular velocity of stator current |
| $k_1, k_2, k_3, k_4, k_5, k_Q, k_t$ | Controller constants                              |
| $H_t, H_m$                          | Inertials of turbine and generator                |
| $v_{sd}, v_{sq}$                    | Stator voltage d and q components                 |
| $v_{rd}, v_{rq}$                    | Rotor voltage d and q components                  |
| $R_s, R_r$                          | Resistances of stator and rotor windings          |
| $L_s, L_r$                          | Self-inductances of rotor and stator              |
| $L_m$                               | Mutual inductance                                 |
| $P_s, Q_s$                          | Stator Active and Reactive Power                  |

## Appendix A

**Table A1.** Parameters and values.

| Parameters and Values |   |
|-----------------------|---|
| Wind turbine          | $V_{\min} = 3 \text{ (m.s}^{-1}\text{)}, V_n = 12 \text{ (m.s}^{-1}\text{)}, V_{\max} = 25 \text{ (m.s}^{-1}\text{)}, P_n = 1.5 \text{ (MW)}$   |
| Power coefficient     | $c_1 = 0.6450; c_2 = 116; c_3 = 0.4; c_4 = 5; c_5 = 21; c_6 = 0.00912; c_7 = 0.08; c_8 = 0.035$   |
| DFIG                  | Rated power 1.5 (MW); Rotor leakage inductance 0.16 (p.u); Rated stator voltage 690 (V); Mutual inductance 2.9 (p.u); Lumped inertia constant 4.32 (s); DC-Link voltage 1150 (V)<br>Friction factor 0.01 (p.u), Pole pairs 3; Stator leakage inductance 0.18 (p.u); Stator resistance 0.023 (p.u); Rotor resistance 0.016 (p.u) |
| PIC                   | $k_{p\omega} = 10; k_{i\omega} = 50; k_{pr} = 10; k_{ir} = 100$ ; Pitch speed ( $k_p = 3; k_i = 30$ ); Pitch power control $k = 200$  |
| SMC                   | $k_d = 10; \lambda = 7; k_q = 5$  |
| ABC                   | $k_\omega = 10; m_\omega = 100; k_{rd} = 5; m_{rd} = 0.8; k_{rq} = 5; m_{rq} = 0.8$ ;   |

## References

- Chojaa, H.; Derouich, A.; Chehaidia, S.E.; Zamzoum, O.; Taoussi, M.; Elouatouat, H. Integral sliding mode control for DFIG based WECS with MPPT based on artificial neural network under a real wind profile. *Energy Rep.* **2021**, *7*, 4809–4824. [\[CrossRef\]](#)
- Chehaidia, S.E.; Abderezzak, A.; Kherfane, H.; Boukhezzar, B.; Cherif, H. An improved machine learning techniques fusion algorithm for controls advanced research turbine (Cart) power coefficient estimation. *UPB Sci. Bull. C* **2020**, *82*, 279–292.
- El Mourabit, Y.; Derouich, A.; Allouhi, A.; El Ghzizal, A.; El Ouanjli, N.; Zamzoumyes, O. Sustainable production of wind energy in the main Morocco's sites using permanent magnet synchronous generators. *Int. Trans. Electr. Energy Syst.* **2020**, *30*, e12390. [\[CrossRef\]](#)
- El-Naggar, M.F.; Mosaad, M.I.; Hasanien, H.M.; AbdulFattah, T.A.; Bendary, A.F. Elephant herding algorithm-based optimal PI controller for LVRT enhancement of wind energy conversion systems. *Ain Shams Eng. J.* **2021**, *12*, 599–608. [\[CrossRef\]](#)
- Mossad, M.I.; Sabiha, N.A.; Abu-Siada, A.; Taha, I.B.M. Application of Superconductors to Suppress Ferroresonance Overvoltage in DFIG-WECS. *IEEE Trans. Energy Convers.* **2021**, *37*, 766–777. [\[CrossRef\]](#)
- Hamane, B.; Doumbia, M.L.; Bouhamida, M.; Draou, A.; Chaoui, H.; Benganem, M. Comparative study of PI, RST, sliding mode and fuzzy supervisory controllers for DFIG based wind energy conversion system. *Int. J. Renew. Energy Res.* **2015**, *5*, 1174–1185.
- Li, P.; Xiong, L.; Wu, F.; Ma, M.; Wang, J. Sliding mode controller based on feedback linearization for damping of sub-synchronous control interaction in DFIG-based wind power plants. *Int. J. Electr. Power Energy Syst.* **2019**, *107*, 239–250. [\[CrossRef\]](#)
- Kelkoul, B.; Boumediene, A. Stability analysis and study between classical sliding mode control (SMC) and super twisting algorithm (STA) for doubly fed induction generator (DFIG) under wind turbine. *Energy* **2021**, *214*, 118871. [\[CrossRef\]](#)
- Chojaa, H.; Derouich, A.; Bourkhime, Y.; Chetouani, E.; Meghni, B.; Chehaidia, S.E.; Yessef, M. Comparative Study of MPPT Controllers for a Wind Energy Conversion System. In *Lecture Notes on Data Engineering and Communications Technologies*; Springer: Singapore, 2022; pp. 300–310.
- Jia, C.; Longman, R.W. An adaptive smooth second-order sliding mode repetitive control method with application to a fast periodic stamping system. *Syst. Control. Lett.* **2021**, *151*, 104912. [\[CrossRef\]](#)
- Li, P.; Xiong, L.; Ma, M.; Huang, S.; Zhu, Z.; Wang, Z. Energy-shaping L2-gain controller for PMSG wind turbine to mitigate subsynchronous interaction. *Int. J. Electr. Power Energy Syst.* **2022**, *135*, 107571. [\[CrossRef\]](#)
- Ghafouri, M.; Karaagac, U.; Karimi, H.; Jensen, S.; Mahseredjian, J.; Faried, S.O. An LQR controller for damping of subsynchronous interaction in DFIG-based wind farms. *IEEE Trans. Power Syst.* **2017**, *32*, 4934–4942. [\[CrossRef\]](#)
- Mokhtari, M.; Khazaei, J.; Nazarpour, D. Sub-synchronous resonance damping via doubly fed induction generator. *Int. J. Electr. Power Energy Syst.* **2013**, *53*, 876–883. [\[CrossRef\]](#)
- Roy, T.K.; Mahmud, M.A. Active power control of three-phase grid-connected solar PV systems using a robust nonlinear adaptive backstepping approach. *Sol. Energy* **2017**, *153*, 64–76. [\[CrossRef\]](#)
- Adekanle, O.; Guisser, M.; Abdelmounim, E.; Aboufatah, M. Integral Backstepping controller combined with High Gain Observer for the optimization of grid-connected Doubly-Fed Induction Generator. In Proceedings of the 2017 International Conference on Wireless Technologies, Embedded and Intelligent Systems (WITS), Fez, Morocco, 19–20 April 2017.
- Chehaidia, S.E.; Abderezzak, A.; Kherfane, H.; Guersi, N.; Cherif, H.; Boukhezzar, B. Fuzzy gain scheduling of PI torque controller to capture the maximum power from variable speed wind turbines. In Proceedings of the 2020 IEEE 2nd International Conference on Electronics Control, Optimization and Computer Science (ICECOCS), Kenitra, Morocco, 2–3 December 2020.
- Karad, S.; Thakur, R. Recent trends of control strategies for doubly fed induction generator based wind turbine systems: A comparative review. *Arch. Comput. Methods Eng.* **2021**, *28*, 15–29. [\[CrossRef\]](#)
- Yunus, A.M.S.; Abu-Siada, A.; Mosaad, M.I.; Albalawi, H.; Aljohani, M.; Jin, J.X. Application of SMES Technology in Improving the Performance of a DFIG-WECS Connected to a Weak Grid. *IEEE Access* **2021**, *9*, 124541–124548. [\[CrossRef\]](#)

19. Hamid, C.; Derouich, A.; Hallabi, T.; Zamzoum, O.; Taoussi, M.; Rhaili, S.; Boukhrachef, O. Performance improvement of the variable speed wind turbine driving a DFIG using nonlinear control strategies. *Int. J. Power Electron. Drive Syst.* **2021**, *12*, 2470. [[CrossRef](#)]
20. Tiwari, R.; Babu, N.R. Recent developments of control strategies for wind energy conversion system. *Renew. Sustain. Energy Rev.* **2016**, *66*, 268–285. [[CrossRef](#)]
21. Poller, M.A. Doubly-fed induction machine models for stability assessment of wind farms. In Proceedings of the Power Tech Conference Proceedings, Bologna, Italy, 23–26 June 2003.
22. Chehaidia, S.E.; Kherfane, H.; Cherif, H.; Abderrezak, A.; Chojaa, H.; Kadi, L.; Boukhezzar, B.; Taoussi, M. An Improved Supervised Fuzzy PI Collective Pitch Angle Control for Wind Turbine Load Mitigation. In *Digital Technologies and Applications*; Springer International Publishing: Cham, Switzerland, 2022.
23. Lan, J.; Patton, R.J.; Zhu, X. Fault-tolerant wind turbine pitch control using adaptive sliding mode estimation. *Renew. Energy* **2018**, *116*, 219–231. [[CrossRef](#)]
24. van Solingen, E.; Fleming, P.A.; Scholbrock, A.; van Wingerden, J.W. Field testing of linear individual pitch control on the two-bladed controls advanced research turbine. *Wind Energy* **2016**, *19*, 421–436. [[CrossRef](#)]
25. Abdullah, M.A.; Yatim, A.H.M.; Tan, C.W.; Saidur, R. A review of maximum power point tracking algorithms for wind energy systems. *Renew. Sustain. Energy Rev.* **2012**, *16*, 3220–3227. [[CrossRef](#)]
26. Mousa, H.H.; Youssef, A.-R.; Mohamed, E.E. State of the art perturb and observe MPPT algorithms based wind energy conversion systems: A technology review. *Int. J. Electr. Power Energy Syst.* **2021**, *126*, 106598. [[CrossRef](#)]
27. Gaillard, A. Système éolien basé sur une MADA: Contribution à l'étude de la qualité de l'énergie électrique et de la continuité de service. Ph.D. Thesis, Université Henri Poincaré-Nancy 1, Nancy, France, 2010.
28. Kumar, D.; Chatterjee, K. A review of conventional and advanced MPPT algorithms for wind energy systems. *Renew. Sustain. Energy Rev.* **2016**, *55*, 957–970. [[CrossRef](#)]
29. Yaakoubi, A.; Amhaimar, L.; Attari, K.; Harrak, M.; EL Halaoui, M.; Asselman, A. Non-linear and intelligent maximum power point tracking strategies for small size wind turbines: Performance analysis and comparison. *Energy Rep.* **2019**, *5*, 545–554. [[CrossRef](#)]
30. Viveiros, C.; Melício, R.; Igreja, J.; Mendes, V. Supervisory control of a variable speed wind turbine with doubly fed induction generator. *Energy Rep.* **2015**, *1*, 89–95. [[CrossRef](#)]
31. Mosaad, M.I.; Abu-Siada, A.; El-Naggar, M.F. Application of superconductors to improve the performance of DFIG-based WECS. *IEEE Access* **2019**, *7*, 103760–103769. [[CrossRef](#)]
32. Pena, R.; Clare, J.; Asher, G. Vector control of a variable speed doubly-fed induction machine for wind generation systems. *Epe J.* **1996**, *6*, 60–67. [[CrossRef](#)]
33. Shang, J.; Nian, X.; Liu, K. Air gap field-oriented vector control strategy for high-power electrically excited synchronous motor based on full-order flux linkage observer. *Sci. Res. Essays* **2014**, *9*, 367–373.
34. Srirattanawichaikul, W.; Premrudeepreechacharn, S.; Kumsuwan, Y. A comparative study of vector control strategies for rotor-side converter of DFIG wind energy systems. In Proceedings of the 2016 13th International Conference on Electrical Engineering/Electronics, Computer, Telecommunications and Information Technology (ECTI-CON), Chiang Mai, Thailand, 28 June–1 July 2016.
35. Ebrahimkhani, S. Robust fractional order sliding mode control of doubly-fed induction generator (DFIG)-based wind turbines. *ISA Trans.* **2016**, *63*, 343–354. [[CrossRef](#)]
36. Hamid, C.; Derouich, A.; Taoussi, M.; Zamzoum, O.; Hanafi, A. An improved performance variable speed wind turbine driving a doubly fed induction generator using sliding mode strategy. In Proceedings of the 2020 IEEE 2nd International Conference on Electronics, Control, Optimization and Computer Science (ICECOCS), Kenitra, Morocco, 2–3 December 2020.
37. Cai, G.; Liu, C.; Yang, D. Rotor current control for a doubly-fed induction generator using a novel nonlinear robust control approach based on extended state observer–backstepping. *Trans. Inst. Meas. Control.* **2015**, *37*, 494–504. [[CrossRef](#)]
38. Belmokhtar, K.; Doumbia, M.L.; Agbossou, K. Novel fuzzy logic based sensorless maximum power point tracking strategy for wind turbine systems driven DFIG (doubly-fed induction generator). *Energy* **2014**, *76*, 679–693. [[CrossRef](#)]
39. Adekanle, O.S.; Guisser, M.; Abdelmounim, E.; Aboufatah, M. Robust integral backstepping control of doubly fed induction generator under parameter variation. *Int. Rev. Autom. Control* **2017**, *10*, 178–185. [[CrossRef](#)]
40. Abo-Khalil, A.G.; Alyami, S.; Sayed, K.; Alhejji, A. Dynamic Modeling of Wind Turbines Based on Estimated Wind Speed under Turbulent Conditions. *Energies* **2019**, *12*, 1907. [[CrossRef](#)]
41. Hung, Y.-H.; Chen, Y.-W.; Chuang, C.-H.; Hsu, Y.-Y. PSO Self-Tuning Power Controllers for Low Voltage Improvements of an Offshore Wind Farm in Taiwan. *Energies* **2021**, *14*, 6670. [[CrossRef](#)]
42. Wu, Y.; Dong, J. Local Stabilization of Continuous-Time T–S Fuzzy Systems with Partly Measurable Premise Variables and Time-Varying Delay. *IEEE Trans. Syst. Man Cybern. Syst.* **2021**, *51*, 326–338. [[CrossRef](#)]
43. Mi, Y.; Hao, X.; Liu, Y.; Fu, Y.; Wang, C.; Wang, P.; Loh, P.C. Sliding mode load frequency control for multi-area time-delay power system with wind power integration. *IET Gener. Transm. Distrib.* **2017**, *11*, 4644–4653. [[CrossRef](#)]